Journal of Materials Chemistry A

ROYAL SOCIETY OF CHEMISTRY

PAPER

View Article Online
View Journal | View Issue

Check for updates

Cite this: J. Mater. Chem. A, 2025, 13, 40349

Impact of engineered dual-scale porosity for application-tailored battery electrodes

Anton B. Resing, [a] Yuanzhi Li [b] and Jörg G. Werner *[abc]

Received 4th August 2025
Accepted 28th October 2025

DOI: 10.1039/d5ta06312d

rsc.li/materials-a

The standard battery electrode contains disorganized and heterogeneous electrolyte-filled porosity, resulting in tortuous ion-transport pathways. When energy-dense batteries are quickly charged or discharged, insufficient ion-diffusion rates in the lithiating electrode result in capacity and energy loss due to underutilized active material and increased overpotential. To realize the full adoption of electric vehicles and enable electric vertical take-off and landing aircrafts, fast lithiation at high energy density is a principal challenge that must be overcome without introducing excessive porosity. Engineered multiscale porosity in the form of low-tortuosity and well-connected porous pathways both in the principle through-plane and the secondary in-plane ion-transport directions are a chemistry-agnostic approach to boost attainable capacity and energy at high lithiation rates. Here, we report such architected electrodes with tunable dual-scale porosity, existing as oriented micron-sized through-plane channels with unity tortuosity and well-connected sub-micron-sized in-plane pathways for efficient ion transport. When rationally coupled together, these transport channels enable 78% capacity retention at 4 C lithiation rates in electrodes with areal capacities over 4 mAh cm^{-2}, relevant total porosities between 0.3–0.6, and volumetric capacities up to 272 mAh cm^{-3}.

Introduction

Lithium-ion batteries (LIBs) continue to be the predominant energy-storage choice across the spectrum of consumer devices.[1] Advances in manufacturing and materials both on the electrode and inactive component level have enabled LIBs to continually increase in energy and power density over the past three decades. More recently, this has contributed to the ongoing mass-market adoption of electric vehicles (EVs) and realization of electric vertical take-off and landing aircrafts (eVTOLs).[2–5] Meanwhile, the general micro-architecture of both the anode and cathode has remained the same: a homogenous and random arrangement of solid particles, polymer binder and the pore volume between them.[6–8] From a geometric perspective, however, tailored engineering of the multiscale battery electrode structure, especially the alignment, spacing, and fraction of pores, can enable further jumps in power and energy density.[9–11] Importantly, such architectural advances can be deployed in tandem with any electrolyte or active material pairing, rendering them material and chemistry agnostic.

High-power or fast-lithiating electrodes require efficient ion transport from their separator to current collector sides (through-plane) to avoid premature lithium-ion depletion and corresponding under-utilization of the active material, as well as detrimental lithium metal plating.[11] Thus, conventional slurry-cast electrodes must be thin, typically below 100 μm, as ion transport meets high through-plane resistance due to tortuous pathways in the randomly arranged pore volume. To decrease their tortuosity and enable thick and fast-lithiating electrodes, the introduction of vertically aligned pore channels is the rational geometric choice.[9,12] Such channels increase the effective through-plane diffusivity by providing an ion-transport highway with a tortuosity of one, independent of electrode thickness. Additionally, for lithium ions to efficiently reach their final destination within the active-material particles located between such channels, secondary inter-particle porosity providing sufficient diffusivity is required.[12]

Electrodes with vertically aligned low-tortuosity channels require specialized fabrication techniques; demonstrated examples include freeze casting, 3D printing, laser ablation, magnetic templating, and phase inversion.[12–16] Through application of these methods, it has been demonstrated that an electrode with aligned channels exhibits improvement in capacity retention at high C-rates over electrodes without this engineered pore space. Many of these techniques, however, result in electrodes with high porosities between 0.6–0.8.[13,15] While such high porosities generally lead to high rate capabilities, these electrodes are unrealistic for deployment in practical LIBs due to their low volumetric active material loading, resulting in cell-level volumetric capacities similar to those of thin-electrode batteries. Additionally, the excess porosity must

[a]Division of Materials Science and Engineering, Boston University, Boston, MA, USA. E-mail: jgwerner@bu.edu
[b]Department of Mechanical Engineering, Boston University, Boston, MA, USA
[c]Department of Chemistry, Boston University, Boston, MA, USA

be filled with electrolyte, adding to the dead weight of the LIB and decreasing its cell-level gravimetric energy.

Previous work in our group introduced hybrid inorganic phase inversion (HIPI), a method inspired by the decades-old manufacture of phase-inversion membranes for water-filtration that is still used today at commercial production levels. HIPI is a material-agnostic technique to structure inorganic particles into low-tortuosity architectures. The execution is practically simple and similar to conventional blade casting but with four main differences: first, the HIPI suspension has a higher polymer fraction (>10 wt%). The polymer is the structure directing component that separates into polymer-lean and polymer-rich phases during phase inversion that result in the pore channels and material dense walls, respectively.[17–19] Second, the cast suspension is immersed for a set time (t_{NS}) in a coagulation bath containing a nonsolvent for the polymer, often water or alcohol, which also exhibits high miscibility with the solvent of the suspension. This is the structure-defining step that provides control over the total porosity (ε_t) and channel density (C_d, channels per mm^2): for example, the nucleation density of the polymer-lean phase (C_d) can be controlled by tailoring the Hansen solubility parameters of the nonsolvent relative to the polymer.[14] Third, a solvent–swollen gel substrate is used instead of a metal foil. We demonstrated that this is critical to ensure that the vertical low-tortuosity channels formed during phase inversion are open and accessible from one side of the electrode (Fig. 1 and S1).[14] Lastly, the architected composite film is pyrolyzed to carbonize the polymer component resulting in a mechanically rigid and electronically conductive electrode. The power of the HIPI process is in the wide range of processing parameters that can be used to control and quench the nonequilibrium and anisotropic structure, resulting in a high degree of tunability across the performance-defining architectural features such as ε_t and C_d.

Our group's previous work reported on the successful HIPI-based fabrication of low-tortuosity lithium titanate (LTO), lithium iron phosphate (LFP), and yttria-stabilized zirconia/nickel oxide composite electrodes.[14] We demonstrated that HIPI-derived LTO and LFP electrodes are electrochemically and mechanically stable in both half- and full-cell configurations. Notably, a full cell of HIPI-derived LTO anode and LFP cathode retained 80% of its capacity after 1000 cycles.[14] The use of related phase-inversion methods was recently expanded to sodium vanadium phosphate and lithium nickel manganese cobalt oxide cathodes, as well as silicon and carbon anodes, demonstrating its material agnostic nature.[20–24]

So far, research on phase-inversion-based low-tortuosity electrodes has focused only on controlling C_d and the geometry of the channel pores. However, limited consideration has been given to ε_t or the balance between the porosities contributed by the channels and the inter-particle pores in the material-dense walls, or the morphology of this secondary porosity. This is a critical omission, since the inter-particle pore space controls in-plane transport from the low-tortuosity through-plane channels into the energy-storing walls. Thus, poor connectivity and high tortuosity of this secondary pore space also contribute to a low effective diffusivity of lithium ions. We propose that the interplay between both scales of porosity as well as their morphology determine the balance of rate capability and energy density in architected electrodes. We believe that a lack of adequate fabrication methods with sufficient control over both pore volumes has so far prevented the experimental assessment of their respective and coupled impact on the lithiation rates of such engineered electrodes with dual-scale porosity.

Here, we present an extensive study on the electrochemical properties of 18 HIPI-derived LTO electrodes with distinct engineered dual-scale porosity of tailored micron-scale channels and sub-micron inter-particle porosity, respectively. We introduce the two diffusion stages inherent to phase inversion as a controlling handle over both scales of porosity. Based on our understanding of the process–structure relationships of HIPI, we are able to fabricate low-tortuosity electrodes with engineered dual-scale pore architecture of tunable volume

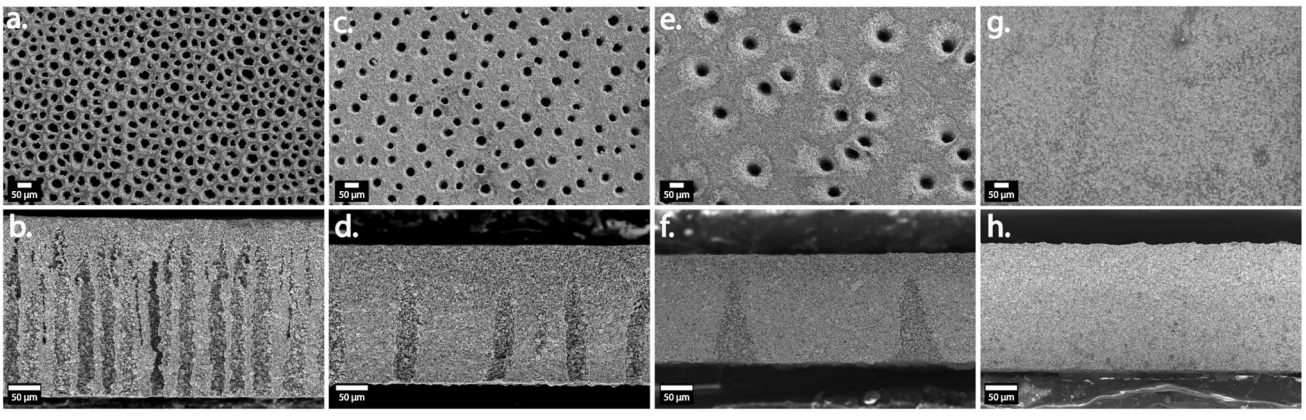

Fig. 1 Scanning electron microscope (SEM) images of HIPI-architected electrodes after cycling with low-tortuosity through-plane channels, whose channel densities (C_d) can be tailored between high (100s of channels per mm^2), medium (~100 mm^{-2}), low (10s mm^{-2}), and no channels. Top view SEM images (a, c, e and g) showing the open and accessible channels and cross-sectional SEM images (b, d, f and h) showing the low-tortuosity nature of the through-plane channels.

fraction (ε_t) between 0.3 and 0.6 that have application-relevant areal capacities and tap densities ranging over 4.3–6.1 mAh cm^{-2} and 0.8–1.6 g cm^{-3}, respectively. This range overlaps with the porosities found in state-of-the-art high-energy commercial electrodes with single-scale porosity (ε_t = 0.2–0.4), allowing for meaningful translation of our findings.[6,8] LTO is used for its structural stability, electrochemical durability, and application in high-power batteries.[14,25,26] Further, LTO's high lithiation potential of 1.55 V *vs.* Li/Li^+ allows us to study the impact of dual-scale porosity on overpotential and capacity loss due to ionic resistance and ion-depletion, respectively, without the risk of lithium plating and related cell degradation. However, we claim that the fabrication technique itself and the conclusions drawn are broadly applicable to other active materials in high-rate electrodes. Thus, our HIPI-derived LTO electrodes with engineered dual-scale porosity serve as a powerful tool to elucidate architecture–performance relationships which can guide the design of tailor-made electrodes that meet application-specific energy and power demands, two performance metrics that are intrinsically coupled through the electrode and pore-space architecture.

Tailored channel density (C_d) across porosity ranges

The HIPI process results in binderless LTO-carbon composite electrodes (80 wt% LTO, 20 wt% carbon) with aligned through-plane channels of tunable density (C_d, channels per mm^2) as shown by the scanning electron microscope (SEM) images in Fig. 1. The separator-facing surfaces exhibit openings (Fig. 1a, c, e and g) to the channels that traverse through the cross-section of the electrode (Fig. 1b, d, f and h) for ion accessibility and transport to the active material particles between the channels (also see Fig. S1). The HIPI processing parameters enable a range of C_d spanning three orders of magnitude: for example, 525 mm^{-2} (Fig. 1a and b), 160 mm^{-2} (Fig. 1c and d), 30 mm^{-2} (Fig. 1e and f), and 0 (Fig. 1g and h). This control of C_d across such a broad range enables systematic studies on the composition–structure–performance relationships of low-tortuosity and dual-porosity architected electrodes. A summary of the HIPI processing parameters and resulting properties of all 18 electrodes discussed here are given in Tables S1 and S2, respectively.

First, the performance dependency on total porosity (ε_t) and C_d is probed by testing six distinct HIPI-architected electrodes which are paired based on similar ε_t but distinct C_d: two electrodes at low ε_t of 0.32 and 0.38 with a C_d of 0 and 200 mm^{-2}, thicknesses of 197 and 217 μm, and LTO loadings of 31.2 and 31.3 mg cm^{-2}, respectively (Fig. 2a and b); two electrodes at medium ε_t of 0.43 and 0.45 with a C_d of 30 and 160 mm^{-2}, thicknesses of 204 and 203 μm, and LTO loadings of 25.5 and 26.9 mg cm^{-2}, respectively (Fig. 2c and d); and two electrodes at high ε_t of 0.54 and 0.59 with a C_d of 205 and 525 mm^{-2}, thicknesses of 227 and 286 μm, and LTO loadings of 24.4 and 27.1 mg cm^{-2}, respectively (Fig. 2e and f). The relative capacity (capacity retention relative to the 0.1 C capacity) of these six electrodes is tested at constant-current lithiation rates up to 4 C, as lithiation is the rate-dominant process. Slower delithiation (0.5 C) is employed to mitigate uneven lithium deposition on the counter electrode of the half cells. Important for quantitative comparison independent of cycle number, all electrodes regain 100% of their original 0.1 C capacity after fast lithiation-rate tests (Fig. 2a, c and e), and the channels remain open and accessible with no observable degradation to the architecture (Fig. 1).

Overall, the electrodes with higher C_d show better capacity retention at increased C-rates for each of the three ranges of ε_t, an indication of their improved ion-transport and accessibility of active material. The C-rate at which the performance enhancement due to higher C_d occurs is correlated with the ε_t of the electrode: for example, at 0.5C, the electrodes with medium and high ε_t show no differences in capacity retention with increasing C_d (Fig. 2c and e). Conversely, the electrodes with low $\varepsilon_t < 0.4$ exhibit a 60% difference in capacity retention from 0.1 to 0.5 C between a C_d of 0 and 200 mm^{-2} (Fig. 2a). At the other end of the porosity spectrum, the electrodes with ε_t between 0.5 and 0.6 show only a 5% improvement in capacity retention even at 2 C despite C_d differing by a factor of 2.5 (Fig. 2e), while at medium and low ε_t, the relative capacity at 2 C is 130% and 270% higher, respectively, with an increase in C_d (Fig. 2a and c). The performance benefit of increasing C_d from 205 to 525 mm^{-2} for the highly porous electrodes ($0.5 < \varepsilon_t < 0.6$) becomes substantial only at a fast lithiation rate of 4 C (Fig. 2e). At this rate, the 525 channels per mm^2 allow a capacity retention of 78%, coming close to meeting the United States Department of Energy's (USDOE) goal of 80% capacity retention during a 15 minutes fast charge of an EV, compared to only 50% for 200 channels per mm^2 at a similar overall porosity.[27] These results lead to two conclusions: (1) high porosity allows for better capacity retention at fast lithiation rates, as is commonly observed, and, most importantly, (2) distributing more porosity into through-plane channels of unity tortuosity at the same total porosity is additionally beneficial for high-rate operation.

While the range of an EV is directly tied to the charged capacity, heat-generation and power consumption during charging is tied to the energy efficiency of anode lithiation. Resistance in the battery will increase the required lithiation voltage (overpotential) and energy, which generates heat that requires mitigation and costs the consumer time and money. Voltage deviation from nominal values can be captured by the mean voltage of operation (μ_v) during a galvanostatic lithiation test. Ohmic resistance and ion kinetics, including charge-transfer and ion-diffusion resistance, contribute to the overpotential and are the cause of μ_v below the operating voltage of a LTO electrode at 1.55 V *vs.* Li/Li^+.[25] A lower μ_v for the LTO half cell during lithiation translates to an increased lithiation charging voltage in a full cell.

We find that across all ranges of ε_t, an increase of C_d results in more energy-efficient lithiation, reflected by μ_v values closer to 1.55 V (Fig. 2b, d and f). For example, electrodes with similar ε_t of 0.59 and 0.54, but different C_d of 525 mm^{-2} and 205 mm^{-2}, exhibit almost identical 2 C lithiation capacity retention (Fig. 2e), but the high-C_d electrode exhibits a μ_v of 1.16 V, while the low-C_d electrode decreases to a μ_v of 1.04 V (Fig. 2f). These overpotentials contribute to relative lithiation energy losses of

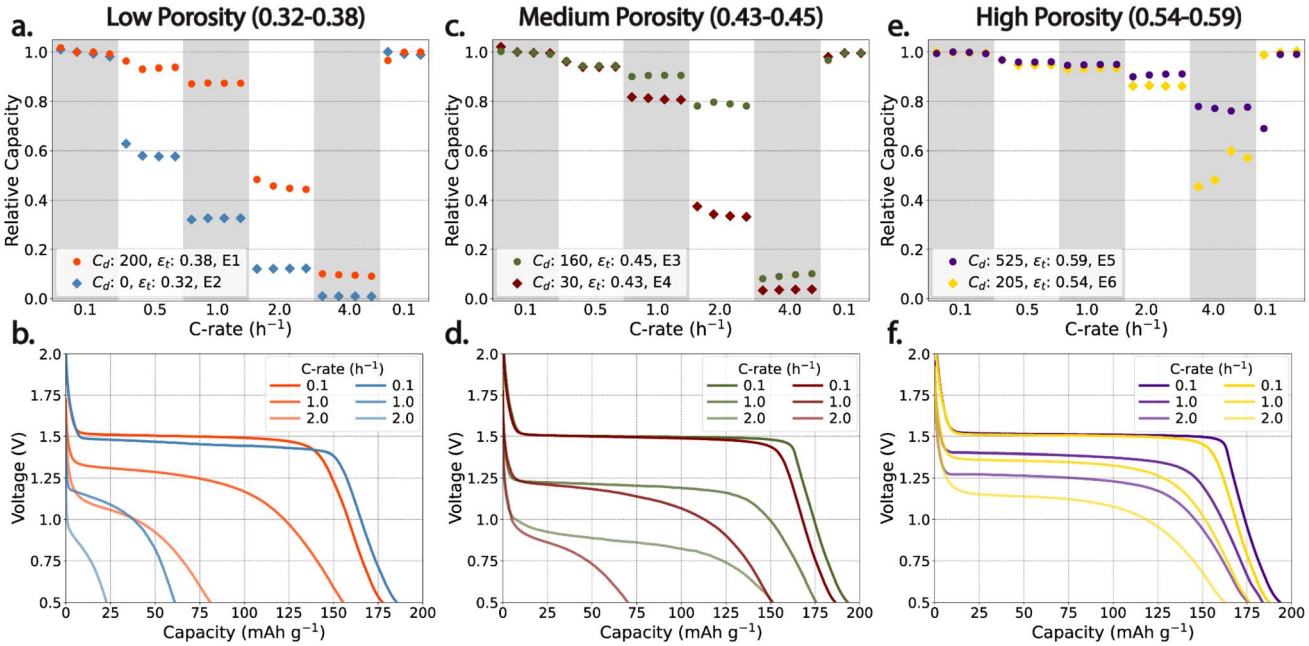

Fig. 2 Galvanostatic lithiation rate performance of architected electrodes across three ranges of total porosity (ε_t), 0.32–0.38 (a and b), 0.43–0.45 (c and d), and 0.54–0.59 (e and f). Each plot in the top row (a, c and e) shows the relative capacity at varied C-rates of an electrode with higher channel density (C_d, channels per mm^2) compared to that of an electrode with lower C_d, demonstrating the critical role that C_d plays in maintaining high-rate performance. The bottom row (b, d and f) shows representative galvanostatic lithiation profiles of the associated top-row plots at 0.1 C, 1 C, and 2 C, demonstrating the increased overpotential induced by ion diffusion resistance in low C_d electrodes across all porosity ranges. Delithiation of all electrodes at 0.5 C. The legends in a, c and e correspond to the electrodes plotted in b, d and f, respectively, and reference the electrode identifier from Tables S1 and S2.

26% and 36%, respectively, at a lithiation rate of 2 C. Thus, the inclusion of more channels at similar total porosity provides more energy-efficient charging, likely limiting heat generation. This beneficial energy effect of high-C_d electrodes is in addition to the higher relative capacity at the faster 4 C lithiation rate. Analogous beneficial energy trends with increased C_d are observed for all ranges of ε_t (Fig. 2b and d). Thus, the fact that 100's of channels per mm^2 can be introduced to electrodes without substantially changing ε_t demonstrates that engineered primary porosity presents an opportunity to increase relative capacity and energy efficiency at high C rates without compromising on the usable energy density of the electrode.

Control over and impact of secondary (inter-particle) porosity

Reducing ε_t from above 0.6 for state-of-the-art phase-inversion battery electrodes to 0.3–0.6 in this report required an understanding of the previously unreported two temporal diffusion stages during phase inversion that define the dual-scale micron and sub-micron ion transport pathways, respectively. While this represents a complicated diffusion problem, HIPI is practically simple: the nonsolvent immersion step initiates the through-plane growth of the polymer-lean phase, which results in the aligned pore channels within around 30 seconds (Fig. 3a).[14,28] This is the first temporal stage where the through-plane diffusional exchange between the solvent in the suspension film and nonsolvent in the surrounding bath dominates. After the aligned liquid-filled channels are formed, the second diffusion stage begins that is typically underappreciated or not considered at all: in-plane solvent/nonsolvent exchange between the liquid-filled channels and the walls rich in polymer and active material. This impactful exchange mechanism controls structure formation of the sub-micron pores within the walls including their connectivity and tortuosity. Phase inversion is often allowed to continue for hours, or the nonsolvent immersion time (t_{NS}) is not even reported, a critical omission for a diffusion-controlled process.[20,29–31] When nonsolvent exchange continues to an equilibrium state, the resulting morphology in the material-rich wall is a sponge-like structure with a large fraction of pore volume (SI Fig. S4). Time, temperature, and nonsolvent type are rational knobs to control the diffusion and extent of solvent/nonsolvent exchange during this second change. For example, by removing the vitrifying film from the nonsolvent bath after channel formation but before the solvent/nonsolvent exchange with the wall has reached its final equilibrium, the polymer is quenched in a gel state with a substantial fraction of remaining solvent. The drying of this solvent-rich gel results in an increased packing density of the active material particles and structure-directing polymer, which in turn results in a dense carbon/particle composite electrode after carbonization (SI Fig. S4 and S5). Thus, early quenching in the HIPI process is an analog to calendaring of a conventional electrode, where ε_t is controlled with t_{NS} analogous to pressure in calendaring. The electrodes achieved in this report with $0.3 < \varepsilon_t < 0.6$ are the result of quenching the phase inversion after 5–180 minutes and controlling the solvent/nonsolvent exchange

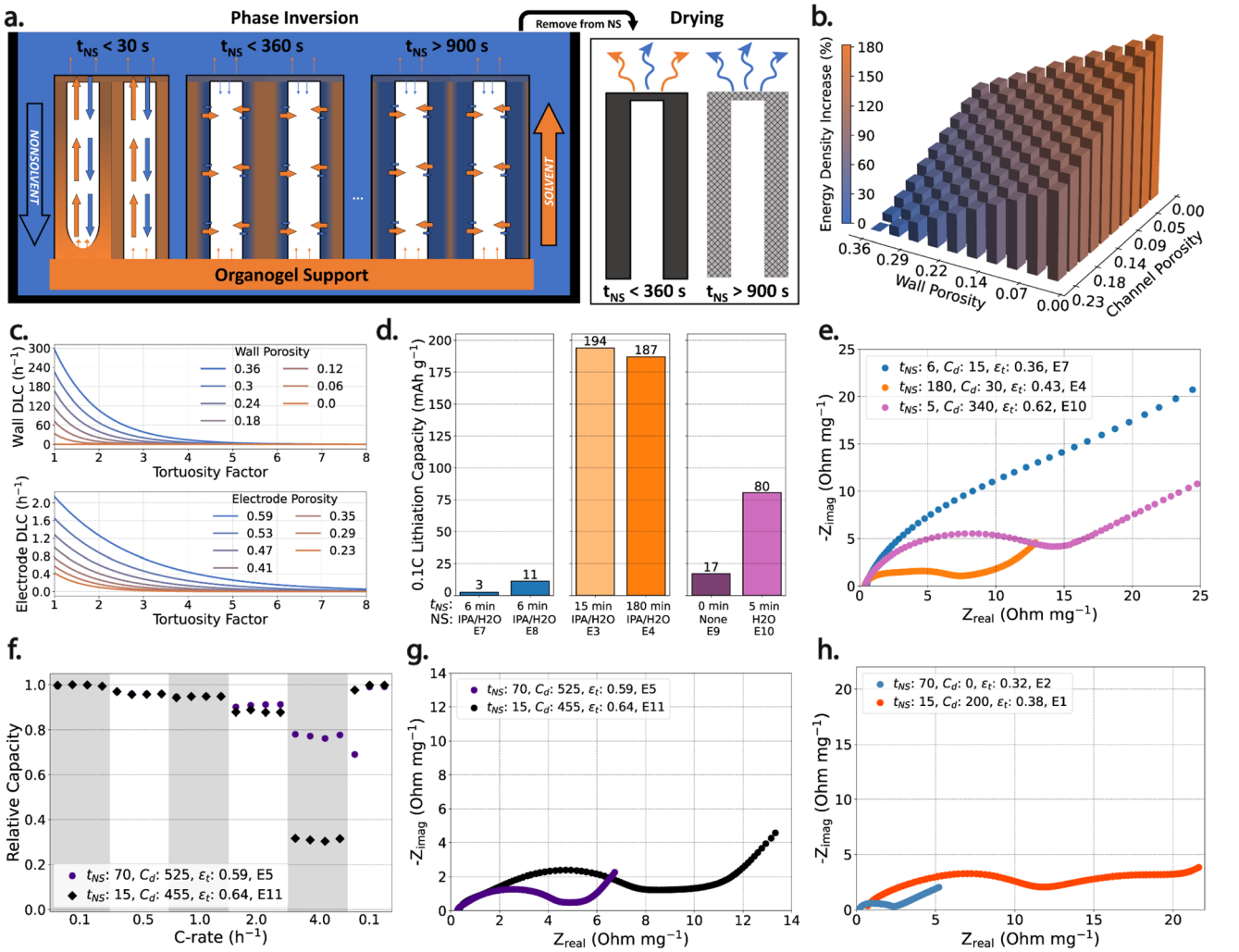

Fig. 3 (a) Schematic illustration of channel-like pore formation through the opposing diffusion of solvent and nonsolvent in phase inversion. When quenched after a short immersion time (t_{NS} < 360 s), the result is a higher fraction of solvent (orange) remaining in the material-dense wall, leading to substantial densification during drying and lower accessibility to the active material. Alternatively, diffusion can be allowed to proceed for longer times (t_{NS} > 900 s), which results in highly porous walls after drying and carbonization. (b) Three-dimensional bar plot demonstrating how energy density increases when independently replacing wall and channel porosity with active material. These calculations are based on the best performing electrode E5 at 4 C as the baseline, which has a $\varepsilon_t = 0.59$ that was divided into a wall porosity of 0.36 and a channel porosity of 0.23 (left corner). (c) The diffusion limited C-rate (DLC) of a single wall (top) and the full electrode (bottom) is plotted against values of tortuosity factor for various wall and electrode total porosities. (d) Bar plot of the experimental 0.1 C lithiation capacity achieved by electrodes with various nonsolvent types, immersion times (t_{NS} in minutes) and channel density (C_d in channels per mm^2). (e) Electrochemical impedance spectroscopy (EIS) presented as a Nyquist plot showing electrodes whose 0.1 C capacity is plotted in the first (E7), fourth (E4) and sixth (E10) column in (d) showing the trend of decreasing resistance with longer t_{NS} and replacement of isopropanol (IPA) with water in the nonsolvent bath. The full and areal Nyquist plots are shown in SI Fig. S2. (f) The relative capacity at varied C rates of two electrodes with similar architecture and different nonsolvent immersion time (t_{NS} in minutes), illustrating the impact that vitrification-induced tortuosity in the secondary porosity has on high-C-rate performance. (g) EIS Nyquist plots of the two electrodes in (f) demonstrating the differing resistance between electrodes with similar C_d and ε_t but different t_{NS} of 70 and 15 minutes. (h) EIS Nyquist plots of two low-porosity electrodes with C_d of 0 and 200 mm^{-2}, respectively, demonstrating the sensitivity of EIS to the local microstructure around the LTO particles but not C_d nor showing a correlation to high-rate lithiation capacity (compare to Fig. 2a). Area normalized EIS Nyquist plots for (g and h) can be found in Fig. S3. The legends in plots (d–h) reference the electrode identifier from Tables S1 and S2.

rate through its dependency on temperature and their identities (details in SI Table S1).

Both C_d and the particle packing within the walls directly determine ε_t and thereby the theoretical volumetric energy density of the electrode (Fig. 3b). For example, electrode E5 with the best performance at 4 C has a ε_t of 0.59 which is divided into fractions of roughly 0.23 in the channels and 0.36 in the walls (Fig. 1a, b and 2c). In a thought experiment, by lowering the wall porosity of this electrode to 0.16 and directly replacing this porosity with active material, the theoretical volumetric energy density of the electrode is increased by 55% (Fig. 3b). Further, decreasing the fraction of channel porosity to 0.13 would result

in an electrode with a ε_t of 0.29 and a 92% energy density increase from the baseline electrode with a ε_t of 0.59. However, in an electrode without engineered porosity, the coupling of porosity to energy and power means that removal of porosity decreases the C rate that an electrode can be lithiated at. This dynamic property can be described by the Diffusion-Limited C Rate (DLC), defined by Heubner *et al.* as the C-rate at which the ion concentration in the electrolyte phase is reduced to zero near the current collector of the lithiating electrode (anode for charging or cathode for discharging).[32] To illustrate this effect, we plot the DLC across a range of reported tortuosity factor values from one to eight that capture the coupled contributions of the primary (channels) and secondary (walls) pores and the variability that may occur due to the distinct structure of the HIPI electrodes (Fig. 3c and SI eqn (S1)).[32–37] Importantly, the DLC for a 20 μm thick wall with a ε_t of 0.36 when taken as a stand-alone thin electrode is two orders of magnitude larger than that of a 286 μm thick electrode with a ε_t of 0.59 without aligned channel pores. These stark differences in DLC suggest that through-plane ion diffusion dominates the lithiation rate limitations, though its coupling to the in-plane diffusion through the secondary pore volume in the walls cannot be omitted, as we show below.

We find that t_{NS} and nonsolvent type do not just have a profound impact on the fraction of secondary pore volume, as described above, but also the accessibility to the active material and the electrode resistance (Fig. 3d and e). For example, a t_{NS} of only six minutes in a weak nonsolvent mixture of isopropanol (IPA) and water (1 : 1 vol%) results in negligible low-rate gravimetric capacity of 3 mAh g^{-1} and 11 mAh g^{-1} for electrodes with a C_d of 15 and 160 mm^{-2}, respectively (Fig. 3d). This inaccessibility of LTO capacity is similar to the 17 mAh g^{-1} capacity measured for an electrode that is directly dried without undergoing phase inversion. In contrast, a longer t_{NS} of 15 minutes and above results in accessibility and full low-rate capacity (Fig. 3d). Electrochemical impedance spectroscopy (EIS) characterization further confirms the high resistance of electrodes from ultrashort t_{NS} in weak nonsolvents, while the slightly longer t_{NS} decreases the resistance by an order of magnitude (Fig. 3e and S2).

The transition in active material accessibility and electrode resistance due to differing t_{NS} must originate from a difference in the morphology of the walls after drying and carbonization that are caused by compositional changes over the first few minutes during phase inversion. We postulate that when a solvent-rich polymer-containing suspension from short t_{NS} is dried, the result is a dense polymer phase between the LTO particles. After thermal treatment, this polymer phase turns into a dense carbon phase with disconnected porosity that blocks ion transport (SI Fig. S4 and S5). Conversely, a t_{NS} of 15 minutes and beyond yields an inter-particle carbon morphology with connected pores that allows for full accessibility of the active material particles (SI Fig. S5). The minimum t_{NS} to achieve full accessibility is further related to the type of nonsolvent and solvent used. For example, when the same suspension is immersed for only 5 minutes in pure water, a stronger nonsolvent for PAN, the resulting electrode exhibits partial accessibility to the active material (80 mAh g^{-1}) and lower resistance compared to the weaker water: IPA nonsolvent at similar t_{NS} (Fig. 3d and e). These results demonstrate that t_{NS} and nonsolvent type have a profound and previously underappreciated effect that dictates the secondary ion-transport pathways and local resistance of phase-inversion electrodes with dual-scale porosity.

Interestingly, while a 15 minutes t_{NS} is sufficient to provide full active material accessibility at low lithiation rates, the accessibility or tortuosity of the sub-micron secondary pore space still evolves at longer phase-inversion times as evidenced by an increase in high-rate lithiation capacities for longer t_{NS}. For example, two electrodes with similar C_d of 455 and 525 and ε_t of 0.64 and 0.59 but from different t_{NS} of 15 and 70 minutes, respectively, exhibit similar relative capacities at rates up to 2 C, but behave distinctly different at 4 C (Fig. 3f). A t_{NS} of 70 minutes yields an electrode with lower resistance that retains a relative capacity of 78% at 4 C, while the electrode with a t_{NS} of 15 minutes exhibits high resistance with a relative capacity of only 31% at the same 4 C rate even though it is more porous (Fig. 3f and g). Thus, in these electrodes with similarly high C_d, the root cause of the relative capacity difference at high rates must be the in-plane resistance to ion movement. This demonstrates that coupled engineering of the primary (through-plane channels) and secondary (inter-particle porosity) are both essential to lower electrode resistance and push the boundary of achievable lithiation rates in energy-dense electrodes.

The EIS-based resistance is sensitive to the local microstructural differences in the walls and appears to be correlated to the lithiation performance due to the dominant local mass-transport limitations in the secondary porosity in the electrodes described above with high C_d (Fig. 3d–g). However, we note that EIS-based resistance is not always an accurate predictor of high-rate performance (capacity retention) and seems to lack some sensitivity to the impact of the through-plane channels. For example, in the low porosity range of ε_t < 0.4, the electrode with a C_d of 200 mm^{-2} outperforms an electrode with a C_d of 0 mm^{-2} in terms of capacity retentions and energy efficiency at rates above 0.1 C (Fig. 2a and b). Yet, EIS measurements show a larger resistance for the electrode with channels, likely due to its short t_{NS} of only 15 minutes (Fig. 3h). Similar seemingly contradictory lithiation performance and EIS-based resistances are also observed for electrodes in the medium porosity range (0.43–0.45) (Fig. 2c, d and S7). Thus, we postulate that EIS-based resistance only captures local phenomena within the walls of HIPI-derived electrodes, but not necessarily the electrode-level ion depletion that evolves over minutes during high-rate lithiation. This depletion effect, however, is a key contributor to cell polarization and incomplete lithiation at high current densities. Thus, we believe that the characterization of electrode-level ion depletion requires different or complementary measurements, such as their voltage relaxation behavior after lithiation shown below.

Voltage relaxation behavior and lithiation rate performance

Local in-plane lithiation gradients in the secondary pore space are difficult to detect even with advanced characterization techniques. Energy dispersive X-ray diffraction and thermal-wave sensing can capture lithium depletion in the electrolyte phase by detecting the resulting through-plane state-of-lithiation (SOL) gradient, showing the highest SOLs near the separator and the lowest near the current collector.[38,39] However, characterizing and quantifying coupled transport phenomena both through- and in-plane in the electrolyte-filled porous regions is important to further the design of high-capacity ultra-fast lithiating electrodes.

Direct quantification of effective diffusivity or the related geometric parameter of tortuosity on the inter-particle scale is difficult. A common yet sometimes misinterpreted method to characterize effective diffusivity in the electrolyte phase is the galvanostatic intermittent titration technique (GITT). This method was initially developed to study solid-state ion transport in dense pellets or disks with little electrolyte percolation to elucidate how diffusion in the solid phase changes with SOL.[40,41] The use of GITT to calculate effective ionic diffusivity of the electrolyte phase does not provide physically relevant values. In thick or high-mass loading electrodes with slow transport kinetics, the addition of aligned transport channels or thinning of the electrode is expected to result in increased effective diffusivity. Since this changes the electrode overpotentials and local electrolyte concentrations near solid active particles, such architectural alterations can change the value of effective diffusivity calculated with GITT.[42–44] Thus, the qualitative trends found by using this technique meet the expectations of an increased effective diffusivity for a thinner electrode or one with aligned transport channels. However, quantitative use of this technique to calculate electrolyte diffusivities is decoupled from physical reality. An alternative method for free-standing electrodes with isotropic porosity is DC-polarization, which treats the electrode as a membrane. By applying current pulses with subsequent relaxation periods, the resistance to ions moving through the membrane can be quantified.[31,45] However, this technique only captures the through-plane resistance and does not provide information on the coupled in-plane diffusion from the channels into the wall, which is especially critical for anisotropic aligned electrodes with hierarchical dual-scale porosity presented in this study.

Here, we evaluate a qualitative technique that captures the open-circuit relaxation dynamics across various SOLs. We demonstrate that the measured relaxation behavior is sensitive to SOL and electrode architecture and, importantly, it can be directly correlated to the relative capacity at C-rates where transport of ions is the rate-limiting step. For example, a 10 minutes lithiation pulse at 1 C is applied to an electrode with a C_d of 200 mm^{-2} and ε_t of 0.38 (E1 in Tables S1 and S2) to develop a through- and in-plane ion-concentration gradient in the liquid electrolyte, followed by chronopotentiometry of the open-circuit (OC) voltage during relaxation. Over six pulses and subsequent relaxation periods, the overpotential during 1 C lithiation increases (Fig. 4a) and the electrode relaxation slows (Fig. 4b and c). The transient relaxation behavior from the end-of-pulse voltage to the equilibrium OC voltage is a combination of ohmic, charge-transfer, and ion relaxation. The voltage responds to ohmic and charge-transfer related resistances quickly, while the relaxation due to ion movement in the liquid and solid phases dominates later relaxation times.[46,47] Ion movement during the relaxation period following fast lithiation can manifest in three ways; diffusion in the solid or electrolyte phase to relax the formed concentration gradients, or diffusion from active material phases with lower electrochemical potentials to those with higher electrochemical potential.[47–49] For example, when local overpotentials are high, as found at higher SOL, lithiation of the carbon phase between the LTO particles is possible. Due to differences in electrochemical potential between the LTO phases and the lithiated carbon phase, ions intercalated in the carbon must move to non-lithiated LTO during OC relaxation. This movement is against the relaxing electrolyte concentration gradient and increases the relaxation time by an order of magnitude (SI Fig. S6). For this electrode with a C_d of 200 mm^{-2} and ε_t of 0.38, the time to relax to 1.5 V grows from 11 to 106 s for SOLs from 17–67% (Fig. 4c) and reaches 810 s at 83% SOL (SI Fig. S6). This jump is likely due to the presence of a lithiated carbon phase at high SOL which redistributes its ions to non-lithiated LTO phases, slowing the relaxation time. The sixth 1 C pulse reaches the 0.5 V cutoff voltage prior to the end of the 10 minutes pulse and relaxes to near 0.9 V (Fig. 4b), likely a coupled effect of carbon lithiation and fully or slightly over-lithiated LTO particles.[25]

Electrodes with engineered porosity show relaxation times that deviate at increased SOLs depending on the arrangement of porosity within the electrode (Fig. 4d). An electrode with a C_d of 525 mm^{-2} and a ε_t of 0.59 shows quick but slowing relaxation times to 1.5 V of 1 s and 15 s at 17% and 67% SOL, respectively (Fig. 4e). A second electrode with a low C_d of 160 mm^{-2} and a moderate ε_t of 0.45 has slower relaxation times of 19 s and 60 s at 17% and 67% SOL, respectively. In comparison, the electrode with a C_d of 200 mm^{-2} and ε_t of 0.38 exhibits a similar relaxation time of 11 s at 17% SOL, but at 67% SOL the relaxation time has increased to 106 s. The relaxation behavior of these three electrodes with varying C_d and ε_t shows a direct correlation to their capacity retention: relaxation times of at 15 s, 60 s, and 106 s at 67% SOL correlate to 2 C relative capacities of 90%, 80%, and 45%, respectively.

To evaluate the effect of C_d on relaxation behavior independent of ε_t, electrode E3 with a C_d of 160 mm^{-2} and a ε_t of 0.45 is compared with electrode E4 that exhibits a C_d of 30 mm^{-2} and a ε_t of 0.43. Electrode E4 is found to have a relaxation time of 120 s at 67% SOL, twice that of electrode E3 (Fig. S8). The fast-relaxing electrode E3 also retains higher relative capacity at rates above 0.5 C (Fig. 2c). We postulate that the dependency of relaxation time on arrangement of porosity is due to SOL gradients both through-plane and in-plane developed during the 1-C pulses. Thus, the pathlength to the non-lithiated LTO gets longer with each subsequent pulse, and the resulting electrolyte concentration gradients get steeper, leading to a longer relaxation time. Additionally, the electrode architecture has a distinct impact on local overpotentials and

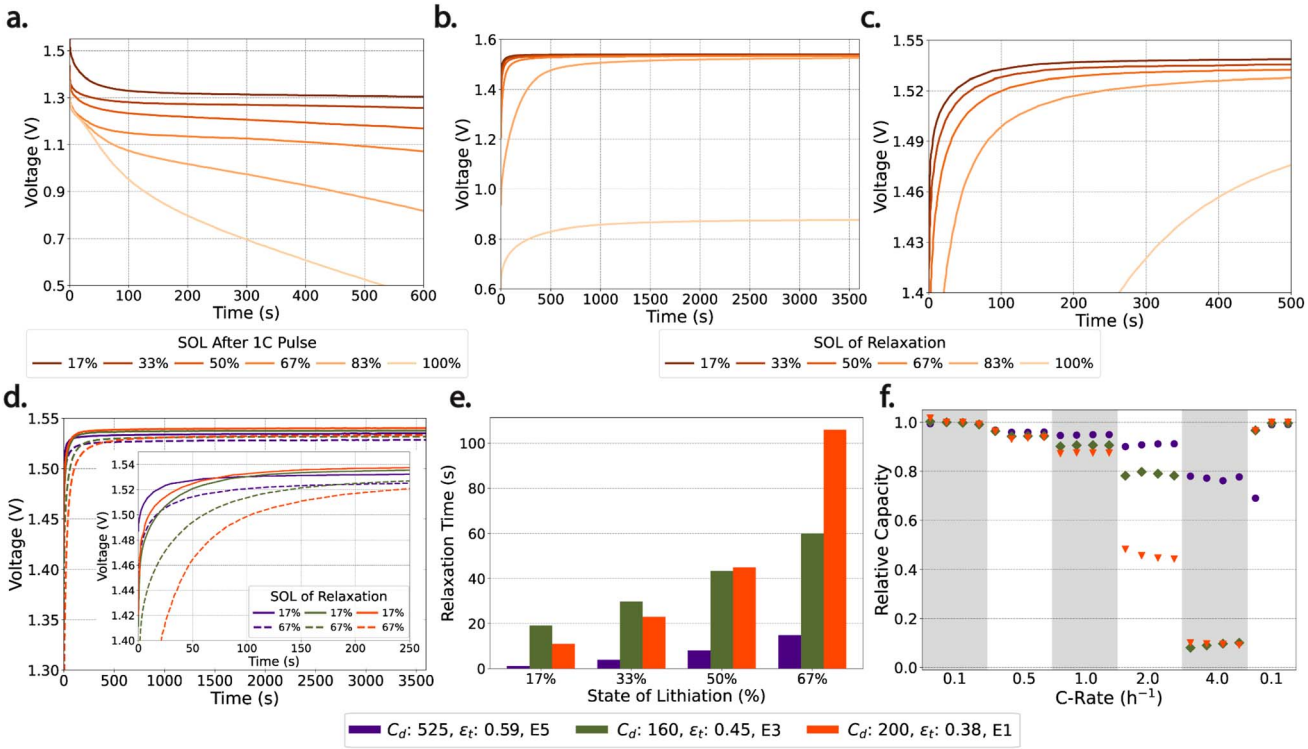

Fig. 4 (a–c) Galvanostatic pulse and voltage relaxation behavior of an electrode with a channel density (C_d) of 200 channels per mm^2 and a total porosity (ε_t) of 0.38. (a) Six galvanostatic 1 C pulses showing the decreasing voltage of lithiation and, (b) the corresponding relaxation profiles after each 1 C pulse showing that after 3600 s of relaxation, the first five pulses all relax to a plateau between 1.52–1.54 V *vs.* Li/Li$^+$. (c) Zoom-in of the voltage *vs.* time relaxation profiles of the first five relaxations between 17% and 83% state-of-lithiation (SOL) illustrating how relaxation slows as SOL increases. (d) Relaxation profiles of three electrodes with different C_d and ε_t at 17% and 67% SOL, illustrating how relaxation is dependent on the architecture of the electrode. (e) Bar plot of relaxation times to 1.5 V *vs.* Li/Li$^+$ for three different electrodes across four SOLs. (f) Relative capacity at varied C-rates of the three electrodes with different relaxation profiles, demonstrating how relaxation time correlates to their high-rate performance. The legends in plots (d–f) reference the electrode identifier from Tables S1 and S2.

the possible lithiation of the carbon phase. This results in distinctly slower relaxation periods following pulses where the cell voltage dropped into the regime where carbon lithiation is electrochemically possible (SI Fig. S6). In summary, the relaxation behavior of electrodes with different arrangements of engineered porosity gives a good qualitative indicator for performance and demonstrates how pore engineering can impact local overpotentials that can lead to lithiating of out-of-equilibrium phases.

Tailored secondary (inter-particle) porosity

As we demonstrated above, electrode performance and relaxation phenomena are tied to both through-plane ion transport, controlled by C_d, as well as in-plane transport dictated by ε_t and the connectivity of the sub-micron secondary pore space in the electrode walls that is influenced by t_{NS} and nonsolvent type. Electrodes with similar C_d but different ε_t show variance in performance, with higher ε_t generally showing better performance at high C rates (SI Fig. S9), as expected. However, tortuosity and ε_t can be decoupled, and secondary porosity with inefficient connectivity and high tortuosity is detrimental to electrode performance (Fig. 3d–g). These results motivate further engineering of the secondary sub-micron pores within the material-dense walls of the HIPI electrodes. To promote low-tortuosity and connected porous networks for fast access to the active material without excessively increasing ε_t, we present two novel approaches based on secondary polymer phase separation of sacrificial porogens during phase inversion: the first approach uses polyvinylpyrrolidone (PVP) along with PAN in the HIPI suspension to form a phase-separating polymer blend between the LTO particles, while the second approach uses a PAN-*b*-PMMA (PMMA: poly(methyl methacrylate)) block copolymer (BCP) as a replacement for the PAN homopolymer to form a microphase-separated inter-particle polymer phase (Fig. 5a). In the case of the PVP/PAN blend, the PVP participates in the phase inversion process, undergoing phase separation from the PAN in the wall followed by PVP dissolution and degradation during thermal treatment. The PVP removal results in connected ion-transport channels within the carbon phase between the LTO particles (SI Fig. S5). In the second case, the PAN-*b*-PMMA BCP goes through microphase separation concurrently with phase inversion. Subsequently, the PAN block is carbonized and the PMMA block is decomposed during the thermal treatment step, leaving behind well-connected nanoscale porosity for faster ion transport (Fig. 5a). We hypothesize that this new mechanism of controlling and introducing

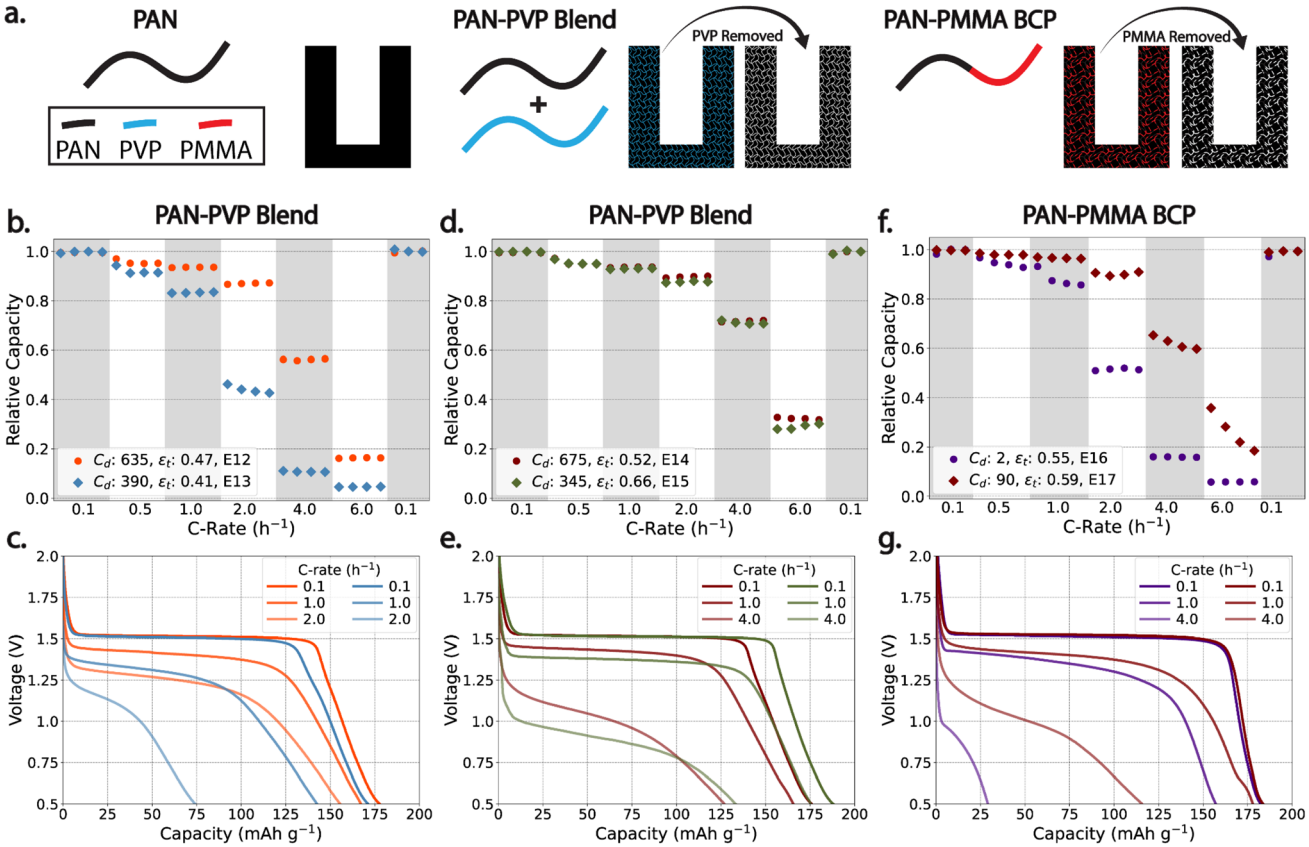

Fig. 5 (a) Shows a schematic illustrating the absence of connected sub-micron pores for short nonsolvent immersion times when pure PAN is used, and the connected sub-micron pores that result from the use of an additional porogen such as a PAN/PVP blend or PAN-*b*-PMMA block copolymer (BCP). (b–g) Shows performance of the electrodes using the PAN/PBP blend with different channel density (b and c) and different PVP fraction (d and e), as well as using the BCP (f and g). All electrodes from ultrashort nonsolvent immersion times t_{NS}. Each plot in the top row (b, d and f) shows the relative capacity of selected electrodes at varied C-rates (h^{-1}). Each plot in the bottom row (c,e and g) shows galvanostatic lithiation profiles of representative cycles. The legends in b, d and f also correspond to plots in c, e and g, respectively. The legends reference the electrode identifier from Tables S1 and S2.

connected secondary porosity to the wall is independent of t_{NS} and, therefore, might allow for short immersion times to achieve low total porosities and high theoretical energy density while ensuring good LTO accessibility.

A PAN/PVP blend with just 10 wt% of a 40 kDa PVP results in electrode E13 with full specific capacity at 0.1 C, even when using an ultrashort t_{NS} of only 6 minutes that results in a low ε_t of 0.41 (Fig. 5b and c). In comparison, electrode E8 obtained from the same nonsolvent type and t_{NS} but without PVP has a similar ε_t of 0.37 and exhibits a specific capacity of only 11 mAh g^{-1} at 0.1 C (Fig. 3d) due to the poor accessibility to its active material. Thus, the addition of just 10 wt% PVP gives full access to the LTO particles, while adding minimal ε_t and maintaining the 8 : 2 weight ratio of active material to conductive carbon, representing efficient engineering of the secondary inter-particle porosity in the walls. This structuring approach of the secondary pore space allows for the architectural boundaries of the HIPI-derived LTO-carbon electrodes to be pushed to lower ε_t. For example, in the pure PAN system, the process conditions to achieve the upper bound of C_d = 525 mm^{-2}, resulted in an ε_t = 0.59, while in the PAN-PVP system an ultra-high C_d = 635 mm^{-2} was enabled at a lower ε_t to 0.47 (E12 in Tables S1 and S2).

In the PAN/PVP system, similar to the pure PAN system, C_d can also be tailored with only small changes to ε_t. For example, electrodes E12 and E13 are fabricated with C_d of 635 and 390 mm^{-2} at a ε_t of 0.47 and 0.41, respectively. Electrode E13 with the lower C_d shows inferior relative capacity at lithiation rates from 0.5 to 6 C, emphasizing the importance of C_d also in electrodes with architected sub-micron porosity (Fig. 5b and c). At 2 C, electrode E12 has a relative capacity of 87%, outperforming the less than 50% relative capacity achieved by electrode E13 with lower C_d. Additionally, the overpotential in the high-C_d electrode E12 at 2 C is similar to that of the low-C_d electrode E13 at 1 C, with μ_v = 1.13 V and 1.16 V, respectively, representing a relative lithiation energy efficiency decrease of 30%. Between these two electrodes, the increase of C_d allows for twice the lithiation speed without any compromise in relative capacity or energy efficiency at relatively small additional overall porosity.

The PAN/PVP blend composition plays a role in the resulting ε_t and tortuosity of the sub-micron pores within the walls of the

electrode. To further probe this, two electrodes with 9 : 1 and 3 : 1 PAN : PVP ratios are fabricated at constant PAN : LTO ratio. The blend with a high fraction of PVP results in an electrode with a C_d of 345 mm^{-2} and a high ε_t of 0.66, while the electrode with the lower PVP fraction results in an electrode with a C_d of 680 mm^{-2} and a ε_t of 0.52. The relative capacity of these two electrodes is very similar at all C-rates up to 6 C (Fig. 5d). Thus, we postulate that the electrode with a C_d of 345 mm^{-2} and a thickness of 315 μm resulting in an areal capacity near 4.6 mAh cm^{-2} exhibits insufficient through-plane transport despite a high ε_t of 0.66. In this electrode, the in-plane ion transport outpaces the through-plane supply due to a surplus of secondary wall porosity. Conversely, in the electrode with a C_d of 680 mm^{-2}, the ε_t of 0.52 is too low to take full advantage of the fast through-plane supply of ions. Additionally, while the two architecturally distinct electrodes show similar relative capacities, there is a distinct difference in μ_v as the C-rate increases (Fig. 5e). At 4 C, the electrode with a lower C_d and higher ε_t results in a μ_v that is 100 mV lower (larger overpotential), illustrating the polarization resistance that results from slow through-plane ion transport at insufficient C_d. In this example, the electrode with a C_d of 345 mm^{-2} and ε_t of 0.66 and the electrode with a C_d of 680 mm^{-2} and ε_t of 0.52 have excess porosity located in the secondary (wall) and primary (channel) pore volumes, respectively. The addition of this excess porosity lowered the energy density while yielding no improvement in power density. These results demonstrate the need for fully elucidated architecture–performance relationships in electrodes engineered with dual-scale porosity and that it is necessary to be deliberate when engineering primary (channels) and secondary (wall) porosity to limit wasted pore space.

Our second pore-engineering approach deploys a PAN-*b*-PMMA BCP to obtain an efficient low-tortuosity secondary pore space within the electrode walls. The resulting HIPI electrodes have a composition of 85 wt% active material and 15 wt% carbon. The BCP works just as effectively as the PAN/PVP blend to promote active material accessibility when short immersion times are used. In this first-reported use of a PAN-*b*-PMMA BCP as the structure directing polymer for phase-inverted electrodes, a range of C_d between 2 and 90 mm^{-2} was achieved. We hypothesize that the limited range of C_d is caused by modified system solubility parameters resulting from the addition of the PMMA block, increasing suspension viscosity and decreasing the thermodynamic driving force for nucleation of the polymer-lean phase during phase inversion. In these electrodes, the trend of a coupled relationship between C_d and relative capacity in electrodes with similar ε_t is maintained, as the BCP derived electrode with a $C_d = 90$ mm^{-2} outperforms the electrode with a $C_d = 2$ mm^{-2}, both in terms of relative capacity and μ_v across C-rates from 1 C to 6 C (Fig. 5f and g).

Summary of relevant structure–performance correlations

Through polymer engineering, we modify the secondary (wall) porosity with sacrificial polymers, while maintaining the highly tailorable channel structure from phase inversion. The additional sub-micron transport pathways provide fast diffusion from the primary (channel) into the secondary (wall) pore volume. To compare application-relevant performance metrics across the vast hierarchical structures presented here, seven HIPI electrodes of distinctly different dual-scale pore design are chosen. Electrodes with high volumetric capacity at low C rates are chosen to compare with those that retain their gravimetric capacity at high C-rates. All electrodes exhibit full active material accessibility at 0.1 C.

Gravimetric and volumetric capacity (Fig. 6a and b). As is commonly observed, electrodes with lower ε_t dropped in gravimetric capacity quicker with increasing C-rate (Fig. 6a). For example, electrode E2 with a ε_t of 0.32 and a C_d of 0 has the highest volumetric capacity and energy at the slowest lithiation rates (Fig. 6b and c). A reasonable application for such an electrode may be grid scale storage, where cost matters most and slow lithiation may be sufficient, making engineered channels unnecessary and likely not cost effective. However, to meet USDOE goals for EVs, a battery must achieve a relative lithiation capacity of 80% during fast charge. With this definition, five electrodes are viable for a 60 minutes charge (1 C), four are viable for a 30 minutes fast charge (2 C), while just one is viable for a 15 minutes ultra-fast charge (4 C) (Fig. 6a). Of the five electrodes capable of a 1 C fast charge, three of them have high volumetric capacities as well, making them the best choice for applications where volumetric density is a constraint and 1 C charging is demanded, such as personal electronics (Fig. 6b). The single electrode that is capable of a 15 minutes fast charge from 0% to 78% SOL is engineered with the PAN homopolymer and has a C_d of 525 mm^{-2}, ε_t of 0.59, and a long t_{NS} of 70 minutes. Thus, promoting both through-plane and in-plane ion transport is critical for a 4 C fast charge. As such, for the PAN/PVP blend electrode with a C_d of 675 mm^{-2} and ε_t of 0.52 to meet the USDOE fast charging goal, we postulate that the rearrangement of primary (channels) porosity into secondary (wall) porosity would be necessary to boost the 4 C relative capacity from 72% to the 80% USDOE goal without increasing ε_t or decreasing the energy density. Conversely, for the PAN-*b*-PMMA BCP electrode with C_d of 90 mm^{-2} and ε_t of 0.59, we postulate that rearrangement of secondary (wall) to primary (channel) porosity is necessary to boost the relative capacity at 4 C from 63% to 80%. Alternatively, thinning of the electrode by reducing overall porosity and without reducing areal capacity also aids through-plane ion diffusion (E18 in Fig. 6b).

Volumetric Energy and Power (Fig. 6c and d). The overpotential added by the ion-transport component of the cell resistance only decreases energy efficiency and increases cost during fast charging of an EV, but not range, as long as the anode remains within a stable electrochemical potential window. However, for applications such as eVTOLs, energy output during fast lithiation of the cathode (discharge of the battery) is a critical metric. This defines the ability of eVTOLs to take off and land safely, when the highest lithiation rates are demanded on the cathode side. The best performing electrode in terms of volumetric energy and capacity across rates > 0.5 C was E18 fabricated with the PAN-*b*-PMMA BCP (Fig. 6b and c). Interestingly, this electrode had a low C_d of 15 mm^{-2}, that, when coupled with efficiently arranged low-tortuosity sub-

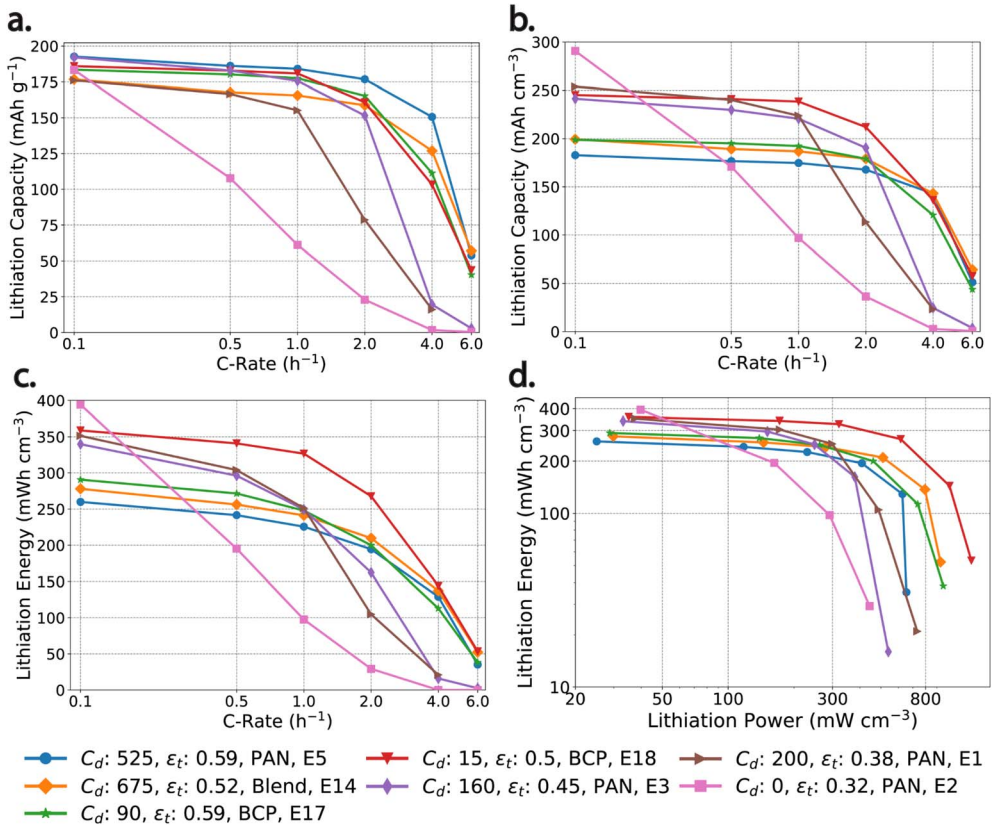

Fig. 6 Overview of application-relevant performance metrics for selected HIPI-architected electrodes. (a) gravimetric lithiation capacity, (b) volumetric lithiation capacity, (c) volumetric lithiation energy, (d) Ragone plot of volumetric energy and power density. All four plots compare seven electrodes, four selected on the basis of good volumetric low C-rate performance and the other three selected based on their high gravimetric C-rate capacity. Legend indicates the channels per mm^2 (C_d), total porosity (ε_t), the polymer type used to fabricate the plotted electrodes, and the electrode identifier from Tables S1 and S2.

micron porosity and 5 wt% less conductive scaffolding, resulted in an active-material-dense electrode with low overpotentials at increased C-rates. This electrode had the best coupled volumetric lithiation energy and power density, retaining 153 mWh cm^{-3} at 1046 mW cm^{-3} (using the transient voltage relative to Li/Li$^+$). The next best coupled performance of 135 mWh cm^{-3} at 790 mW cm^{-3} was realized by an electrode with a C_d of 675 mm^{-2} and ε_t of 0.52 fabricated with a PVP/PAN blend (Fig. 6d).

Conclusions

The demand for electrodes with high retention of capacity and energy at high power or current densities is widespread. To meet future demands of fast lithiation, we must improve upon conventional cathodes used in eVTOLs and anodes for fast-charging needs in EVs, for example. This requires both a fundamental understanding of the impact of various scales of porosities in thick energy-dense electrodes as well as manufacturing methods with control over these multi-scale structures. For example, currently deployed lithium-ion batteries with carbon-based anodes require over one hour to recharge from 0 to 100%, while "fast charging" is typically limited to SOL increases of only 50–60% (*e.g.*, from 20–80% SOL).[50,51] Importantly, these numbers apply to electrodes with thicknesses well below 100 μm, though thicker electrodes are required for high energy density on the cell level by reducing the fraction of necessary but inactive components such as current collectors and the separator. Thus, to improve electrode-level mass transport over 100+ μm without sacrificing lithiation rate for energy density, it is necessary to move from random to aligned porosity in battery electrodes, with geometric optimization of dual-scale engineered porosity as a rational choice.

HIPI can achieve this by exploiting the two temporal diffusion regimes during phase inversion that couple the channel formation and electrode densification, respectively, into one step. Specifically, we introduce here that by controlling the second diffusion regime (minutes) and through the addition of sacrificial polymer porogens on top of the previously demonstrated tunable channel density (seconds), electrodes with tailored dual-scale engineered porosity are achievable. We demonstrate that by modifying HIPI electrodes with sub-micron pores for efficient transport, dense volumetric packing of active material and high volumetric performance at appreciable C rates is enabled. This proves that sub-micron transport pathways play an important role in the coupled volumetric lithiation energy and power densities in architected electrodes. Through dual-scale control over engineered porosity, we highlight the importance of elucidating architecture–composition–

performance relationships to enable the deployment of only the necessary primary and secondary porosity for a given application.

Some of our HIPI-derived electrodes with through-plane and in-plane ion-transport highways approach the ε_t of conventional slurry cast electrodes, which are roll-to-roll processed and require a calendaring step to achieve a high volumetric active-material density. In principle, HIPI is well suited for facile integration into a manufacturing line for electrode fabrication at scale, as phase inversion already exists as a commercial roll-to-roll process. However, the high temperature carbonization step, used here to add conductivity to the electrodes, may limit manufacturing at scale. Thus, future work should focus on integrating conductive carbon additives into the slurry suspension for HIPI and similarly study their relationships between dual-scale porosity, rate performance, and energy density. More broadly, the rate-limitation of high-capacity electrodes from any active material is most often governed by electrolyte-level ion transport, which is dictated by the architectural features of primary and secondary porosity in thick dual-scale engineered electrodes. Thus, the geometric architecture–performance relationships obtained in this report should be in principle transferrable to other active materials as well.

Methods

Suspension preparation

Polymer solutions are composed of dimethyl sulfoxide (DMSO, Sigma-Aldrich), dimethylformamide (DMF, Sigma-Aldrich), deionized water (Millipore Milli-Q, 18.2 MΩ cm) and either a homopolymer poly(acrylonitrile) (PAN, Sigma-Aldrich, M_w = 150 000), a polymer blend of PAN and polyvinylpyrrolidone (PVP, Sigma-Aldrich, M_w = 1 300 000 or M_w = 40 000), or a block copolymer (BCP) of PAN and (poly(methyl methacrylate)) (PMMA). These mixtures were stirred at 80 °C and 200 rpm until dissolved.

Separately, lithium titanate ($Li_4Ti_5O_{12}$, LTO, MTI Corp.) with a reported D10, D50 and D90 particle size of 0.2–0.6 μm, 0.9–1.8 μm and ≤10 μm, respectively, was mixed with DMSO and dispersed with 10 minutes of sonication and vortex stirring, repeated three times. The LTO dispersion was then added to PAN, PAN-*b*-PMMA and PAN/PVP solutions to form the HIPI precursor suspension, detailed ratios of the suspensions can be found in SI Table S1.

Block copolymer synthesis

PAN-*b*-PMMA block copolymer was synthesized *via* reversible addition-fragmentation chain-transfer (RAFT) polymerization. Detailed procedure has been described elsewhere.[52,53] Briefly, purified methyl methacrylate (MMA, Sigma-Aldrich, 99%, contains ≤30 ppm MEHQ as inhibitor), 4-cyano-4-(phenylcarbonothioylthio)pentanoic acid (CPADB, Sigma-Aldrich) and 2,2′-azobis(2-methylpropionitrile) (AIBN, Sigma-Aldrich, 98%) were dissolved in benzene in a Schelenk flask. The mixture was freeze-pump-thawed three times using a high-vacuum Schlenk line before being placed in a 60 °C oil bath for 24 h. The resulting PMMA macro-chain transfer agent (macro-CTA) was precipitated in ice-water-cooled methanol and dried under vacuum for 12 h. The purified PMMA macro-CTA was mixed with acrylonitrile (AN, Sigma-Aldrich, ≥99%, contains 35–45 ppm monomethyl ether hydroquinone as inhibitor), AIBN and DMSO. The mixture was freeze-pump-thawed three times and immersed in a 65 °C oil bath for 24 h. Subsequently, two cycles of precipitation into cold methanol, filtration, and redissolving were conducted to yield PAN-*b*-PMMA, which has a composition of 37 wt% PMMA and 63 wt% PAN as calculated from Proton-Nuclear Magnetic Resonance (^{1}H-NMR) spectroscopy (SI Fig. S10).

Preparation of solvent swollen casting support

The organogel support was prepared by mixing 2,2′-(ethylenedioxy)diethanethiol (Sigma-Aldrich), pentaerythritol tetrakis(3-mercaptopropionate) (Sigma-Aldrich), tri(ethylene glycol) divinyl ether (Sigma-Aldrich) at a stoichiometric ratio of thiol to vinyl end groups. 2-Hydroxy-2-methylpropiophenone (Sigma-Aldrich) was added at 1.4 wt% as a photoinitator and 55 wt% NMP was added to swell the organogel. 800 μl of the solution was then pipetted on a glass microscope slide (25 × 75 mm^2) to coat it, followed by exposure to a UV lamp (OmniCure LX500) at a wavelength of 365 nm for 3 minutes to form the organogel.

Electrode casting process

The HIPI precursor suspension was spread with a doctor blade (BYK-Gardener) on an NMP-swollen organogel immediately following UV treatment at a prescribed height. Following spreading, the cast suspension was submerged in a nonsolvent bath, detailed composition and immersion times can be found in SI Table S1 and S2. The free-standing phase-inverted LTO-polymer hybrid is detached from the organogel support and removed from the nonsolvent bath after a defined time (t_{NS}).

Electrode preparation

The composite films composed of polymer and LTO particles were cut into a chosen geometry and dried at 80 °C under vacuum for 12 h. To prevent deformation during thermal treatment, the composite films were sandwiched between two graphite sheets (McMaster). This assembly was placed in a tube furnace (Thermo Fischer Scientific Lindberg Blue M) and treated at 250 °C under air for 2 h to cyclize the PAN, then heated to 750 °C under Ar to carbonize the PAN and remove the PMMA and any residual PVP. Battery electrodes were then transferred into an argon-filled glove box (O_2 < 0.5 ppm, H_2O < 0.5 ppm) prior to coin cell assembly.

Electrochemical measurements

2032-Coin cells (MTI LIR2032, 316 stainless steel) were assembled in a half-cell configuration with a free-standing HIPI-architected LTO/carbon working electrode paired with a lithium metal counter/reference electrode (MTI, thickness = 0.6 mm, diameter = 16 mm), similar to the architecture of

previous reported coin cells.[54] While rarely mentioned in literature, when testing the performance of high areal capacity electrodes while using the standard lithium metal counter/reference electrode, it is important to minimize impacts of the lithium metal electrode on ion diffusion by keeping the metal layer dense with minimal dead lithium at the lithium–separator interface. To promote stability of the lithium metal, we use an electrolyte composed of 1 M lithium bis-trifluoromethanesulfonimide (LiTFSI, Sigma-Aldrich) and 0.08 M lithium nitrate ($LiNO_3$, Thermo Fischer Scientific), dissolved in a 1 : 1 vol% mixture of 1,3-dioxolane (DOL, Sigma-Aldrich) and 1,2-dimethoxyethane (DME, Sigma-Aldrich) which has been shown to improve the performance and morphology of the lithium metal electrode. During assembly the electrodes and a trilayer polypropylene/polyethylene/polypropylene separator (Celgard 2320) were wet with an excess of electrolyte and together with the lithium metal crimped to 1000 psi in a hydraulic crimper (MSE Supplies). The LTO: lithium half-cells were then tested in galvanostatic mode between 0.5–2.5 V *vs.* Li/Li^+ at ambient temperatures between 20–22 °C, on BST8-WA (MTI), BST8-A6V0 (MTI) or CT-4008T-5V10 mA (Neware). First LTO : Li half-cells are cycled at 0.05 C and 0.1 C for break-in, next electrochemical impedance spectroscopy (EIS) measurements were conducted on a Gamry reference 600+ potentiostat with a signal amplitude of 50 mV around the open circuit potential over a frequency range of 0.1 Hz to 1 MHz. Then relaxation phenomena was probed by applying seven 1 C lithiation pulses, with each pulse followed by a two-hour open-circuit relaxation period. With relaxation time defined as the time it took for the open-circuit-voltage to reach 1.5 V after the pulse ended. To further minimize the formation of lithium metal morphologies detrimental to diffusion, we plate (LTO delithiation) at a maximum galvanostatic rate of 0.5 C, and strip (LTO lithiation) across a range of C-rates up to 6 C to test the performance of HIPI electrodes, which are rate limited due to diffusion upon lithiation. The C-rate is determined by the mass of LTO in the electrode and a theoretical gravimetric capacity of 175 mAh g^{-1}. Lithiation energy is determined by integrating the discharge (lithiation) curves (capacity *vs.* voltage), which includes energy costs both due to premature lithium depletion and overpotential.

Electrode characterization

Scanning electron microscopy (SEM) was performed post-mortem on the electrodes. After electrochemical testing, coin cells were disassembled and electrodes were washed with fresh DME. SEM imaging of the post-mortem electrodes was done on a Phenom ProX Desktop scanning electron microscope (Thermo Fischer Scientific) at accelerating voltages of 10 kV. To gather measurements of channel density (C_d), SEM images of the channel openings are segmented in ImageJ by a threshold brightness to distinguish between channel pores and the active material dense matrix. Due to the geometry of the channels the areal ratio at the surface can be used to describe the overall volumetric ratio between channels pores.

Author contributions

ABR and JGW conceptualized and designed the research plan. ABR performed all electrode fabrication, characterization, and formal analysis. YL synthesized the custom block copolymer. AR wrote the first draft of the manuscript. AR and JGW revised the manuscript for publication. JGW supervised the research project.

Conflicts of interest

There are no conflicts to declare.

Data availability

This data is also available from the authors upon reasonable request.

All data supporting the findings of this study are contained within the article and the supplementary information (SI). Supplementary information: overview tables summarizing processing conditions and properties of all 18 electrodes, additional mass- and area-normalized EIS Nyquist plots, additional SEM images for high and low wall porosity, summary plots of relaxation times, ^{1}H-NMR of PAN-*b*-PMMA BCP. See DOI: **https://doi.org/10.1039/d5ta06312d**.

Acknowledgements

The authors acknowledge funding from the Boston University Institute for Global Sustainability and College of Engineering through their Dean's Catalyst Award Program.

References

1 *Executive Summary National Blueprint For Lithium Batteries 2021–2030*, 2021.
2 N. Nitta, F. Wu, J. T. Lee and G. Yushin, *Mater. Today*, 2015, **18**, 252.
3 M. Li, J. Lu, Z. Chen and K. Amine, *Adv. Mater.*, 2018, **30**, 1800561.
4 M. Weiss, R. Ruess, J. Kasnatscheew, Y. Levartovsky, N. R. Levy, P. Minnmann, L. Stolz, T. Waldmann, M. Wohlfahrt-Mehrens, D. Aurbach, M. Winter, Y. Ein-Eli and J. Janek, *Adv. Energy Mater.*, 2021, **11**, 2101126.
5 V. Viswanathan, A. H. Epstein, Y.-M. Chiang, E. Takeuchi, M. Bradley, J. Langford and M. Winter, *Nature*, 2022, 601.
6 F. J. Günter and N. Wassiliadis, *J. Electrochem. Soc.*, 2022, **169**, 030515.
7 M. Ank, A. Sommer, K. A. Gamra, J. Schöberl, M. Leeb, J. Schachtl, N. Streidel, S. Stock, M. Schreiber, P. Bil, C. Allgäuer, P. Rosner, J. Hagemeister, M. Rößle, R. Daub and M. Lienkamp, *J. Electrochem. Soc.*, 2023, **170**, 120536.
8 S. Stock, J. Hagemeister, S. Grabmann, J. Kriegler, J. Keilhofer, M. Ank, J. L. S. Dickmanns, M. Schreiber, F. Konwitschny, N. Wassiliadis, M. Lienkamp and R. Daub, *Electrochim. Acta*, 2023, **471**, 143341.

9 C.-H. Hung, S. Allu and C. L. Cobb, *J. Electrochem. Soc.*, 2025, **172**, 010513.
10 F. L. E. Usseglio-viretta, W. Mai, A. M. Colclasure, M. Doeff, E. Yi and K. Smith, *Electrochim. Acta*, 2020, **342**, 136034.
11 Z. Ju, X. Xu, X. Zhang, K. U. Raigama and G. Yu, *Chem. Eng. J.*, 2023, **454**, 140003.
12 J. S. Sander, R. M. Erb, L. Li, A. Gurijala and Y. Chiang, *Nat. Energy*, 2016, **1**, 16099.
13 J. Wu, Z. Ju, X. Zhang, C. Quilty, K. J. Takeuchi, D. C. Bock, A. C. Marschilok, E. S. Takeuchi and G. Yu, *ACS Nano*, 2021, **15**, 19109.
14 A. B. Resing, C. Fukuda and J. G. Werner, *Adv. Mater.*, 2023, **35**, 2209694.
15 X. Li, S. Ling, L. Zeng, H. He, X. Liu and C. Zhang, *Adv. Energy Mater.*, 2022, **12**, 2200233.
16 K. H. Chen, M. J. Namkoong, V. Goel, C. Yang, S. Kazemiabnavi, S. M. Mortuza, E. Kazyak, J. Mazumder, K. Thornton, J. Sakamoto and N. P. Dasgupta, *J. Power Sources*, 2020, **471**, 228475.
17 G. R. Guillen, Y. Pan, M. Li and E. M. V. V. Hoek, *Ind. Eng. Chem. Res.*, 2011, **50**, 3798.
18 H. Strathmann and K. Kock, *Desalination*, 1977, **21**, 241.
19 H. Strathmann, K. Kock, P. Amar and R. W. Baker, *Desalination*, 1975, **16**, 179.
20 Z. Lv, M. Yue, M. Ling, H. Zhang, J. Yan, Q. Zheng and X. Li, *Adv. Energy Mater.*, 2021, **11**, 2003725.
21 P. Karanth, M. Weijers, P. Ombrini, D. Ripepi, F. Ooms and F. M. Mulder, *Cell Rep. Phys. Sci.*, 2024, **5**, 101972.
22 N. P. Jimenez, M. P. Balogh and I. C. Halalay, *J. Electrochem. Soc.*, 2021, **168**, 040507.
23 W. Wang, A. B. Resing, K. A. Brown and J. G. Werner, *Adv. Mater.*, 2024, **36**, 1.
24 W. Wang, Y. Li, A. B. Resing, J. Yan, Z. Zheng and J. G. Werner, *J. Mater. Chem. A*, 2025, **13**, 29050.
25 B. Zhao, R. Ran, M. Liu and Z. Shao, *Mater. Sci. Eng., R*, 2015, **98**, 1.
26 N. Takami, H. Inagaki, Y. Tatebayashi, H. Saruwatari, K. Honda and S. Egusa, *J. Power Sources*, 2013, **244**, 469.
27 VT Office, *Batteries 2020 Annual Progress Report*, 2020.
28 G. R. Guillen, G. Z. Ramon, H. P. Kavehpour, R. B. Kaner and E. M. V. V Hoek, *J. Membr. Sci.*, 2013, **431**, 212.
29 J. Wu, Z. Ju, X. Zhang, K. J. Takeuchi, A. C. Marschilok, E. S. Takeuchi and G. Yu, *Nano Lett.*, 2021, **21**, 9339.
30 C. T. C. Wan, R. R. Jacquemond, Y. M. Chiang, K. Nijmeijer, F. R. Brushett and A. Forner-Cuenca, *Adv. Mater.*, 2021, **33**, 2006716.
31 J. Wu, Z. Ju, X. Zhang, X. Xu, K. J. Takeuchi, A. C. Marschilok, E. S. Takeuchi and G. Yu, *ACS Nano*, 2022, **16**, 4805.
32 C. Heubner, M. Schneider and A. Michaelis, *Adv. Energy Mater.*, 2020, **10**, 1902523.
33 M. Ebner, D. Chung, R. E. García and V. Wood, *Adv. Energy Mater.*, 2014, **4**(5), 1301278.
34 D. Kehrwald, P. R. Shearing, N. P. Brandon, P. K. Sinha and S. J. Harris, *J. Electrochem. Soc.*, 2011, **158**, A1393.
35 L. Holzer, P. Marmet, M. Fingerle, A. Wiegmann, M. Neumann and V. Schmidt, *Tortuosity and Microstructure Effects in Porous Media*, Springer, 2023.
36 F. L. E. Usseglio-viretta, A. Colclasure, A. N. Mistry, K. Pierre, Y. Claver, F. Pouraghajan, D. P. Finegan, T. M. M. Heenan, D. Abraham, P. P. Mukherjee, D. Wheeler, P. Shearing, S. J. Cooper and K. Smith, *J. Electrochem. Soc.*, 2018, **165**, A3403.
37 F. L. E. Usseglio-Viretta, D. P. Finegan, A. Colclasure, T. M. M. Heenan, D. Abraham, P. Shearing and K. Smith, *J. Electrochem. Soc.*, 2020, **167**, 100513.
38 Y. Zeng, D. Chalise, Y. Fu, J. Schaadt, S. Kaur, V. Battaglia, S. D. Lubner and R. S. Prasher, *Joule*, 2021, **5**, 2195.
39 K. P. C. Yao, J. S. Okasinski, K. Kalaga, I. A. Shkrob and D. P. Abraham, *Energy Environ. Sci.*, 2019, **12**, 656.
40 W. Weppner and R. A. Huggin, *J. Electrochem. Soc.*, 1977, **124**, 1569.
41 S. D. Kangz and W. C. Chueh, *J. Electrochem. Soc.*, 2021, **168**, 120504.
42 J. Wang, M. Wang, N. Ren, J. Dong, Y. Li and C. Chen, *Energy Storage Mater.*, 2021, **39**, 287.
43 H. Gao, Q. Wu, Y. Hu, J. P. Zheng, K. Amine and Z. Chen, *J. Phys. Chem. Lett.*, 2018, **9**, 5100.
44 Y. Zhang, Y. Xiao, L. Chen and S. Hu, *J. Mater. Chem. A*, 2024, **12**, 16537.
45 I. V. Thorat, D. E. Stephenson, N. A. Zacharias, K. Zaghib, J. N. Harb and D. R. Wheeler, *J. Power Sources*, 2009, **188**, 592.
46 T. L. Kirk, C. P. Please and S. J. Chapman, *J. Electrochem. Soc.*, 2021, **168**, 060554.
47 M. M. Hantel, T. Kaspar, R. Nesper, T. F. Fuller, M. Doyle and J. Newman, *J. Electrochem. Soc.*, 1994, **141**, 982.
48 C. Uhlmann, J. Illig, M. Ender and R. Schuster, *J. Power*, 2015, **279**, 428.
49 A. Klein, P. Axmann and M. Wohlfahrt-mehrens, *J. Electrochem. Soc.*, 2016, **163**, A1936.
50 Volta Foundation, *The Battery Report 2024*, 2025.
51 Y. Dong, C. Liu, M. Rui, X. Zhang, Y. Guan, L. Chen, Q. Huang, M. Wang, Y. Su, F. Wu and N. Li, *Adv. Funct. Mater.*, 2025, 2506190.
52 Z. Zhou and G. Liu, *Small*, 2017, **13**, 1603107.
53 Z. Zhou, T. Liu, A. U. Khan and G. Liu, *Sci. Adv.*, 2019, **5**, eaau6852.
54 V. Murray, D. S. Hall and J. R. Dahn, *J. Electrochem. Soc.*, 2019, **166**, A329.

